JGR Atmospheres

RESEARCH ARTICLE
10.1029/2024JD042217

The Response of Tropical Cyclone Inner Core and Outer Rainband Precipitation to Warming in Idealized Convection-Permitting WRF

Alyssa M. Stansfield[1,2] and **Kristen L. Rasmussen**[2]

[1]Department of Atmospheric Sciences, University of Utah, Salt Lake City, UT, USA, [2]Department of Atmospheric Science, Colorado State University, Fort Collins, CO, USA

Key Points:

- Tropical cyclones (TCs) in idealized model simulations produce greater precipitation increases in the inner core (IC) than outer rainbands with warming
- Convective regions occupy a greater areal percentage in the TC IC with warming, which leads to large increases in precipitation
- With warming, the TC cloud base heights decrease and melting levels rise, creating more volume for warm rain processes

Supporting Information:

Supporting Information may be found in the online version of this article.

Correspondence to:

A. M. Stansfield,
alyssa.stansfield@utah.edu

Citation:

Stansfield, A. M., & Rasmussen, K. L. (2025). The response of tropical cyclone inner core and outer rainband precipitation to warming in idealized convection-permitting WRF. *Journal of Geophysical Research: Atmospheres*, *130*, e2024JD042217. https://doi.org/10.1029/2024JD042217

Received 12 AUG 2024
Accepted 28 JAN 2025

Abstract Global mean and extreme tropical cyclone (TC) precipitation have been increasing over the past few decades and are expected to continue to increase into the future due to climate change. Most projections of future TC precipitation use climate models with grid spacings of 25–100 km, which are too coarse to resolve the convective structures and small-scale precipitation processes within TCs. This work uses convection-permitting Weather Research and Forecasting model simulations to investigate how precipitation and precipitation processes change in the inner core (IC) and outer rainbands (OR) of TCs in response to sea surface temperature (SST) warming. The simulations are idealized, with single TCs initialized from weak vortices over domain-constant SSTs. In these simulations, TC intensity and IC precipitation greatly increase with SST warming while OR precipitation increases slightly. A greater area in the IC is occupied by deep convection more frequently in the warmer simulations, while the deep convective activity remains relatively constant with warming in the TC OR. Mixing ratios of hydrometeors and cloud ice increase with warming in both the IC and OR, while the TCs' vertical circulations deepen, melting levels rise, and mean upward velocities strengthen. This work demonstrates how analysis of three-dimensional storm structures can provide insight into processes that change TC precipitation in different regions of the storm, and future work will include applying this analysis to more realistic convection-permitting simulations.

Plain Language Summary Tropical cyclones (TCs) produce large amounts of rainfall that can cause dangerous hazards when these storms make landfall, such as flash flooding and landslides. Rainfall in TCs has increased since 1998 according to data from satellites and is expected to increase in the future based on climate models. However, much of the information about future TC rainfall changes comes from climate models with relatively coarse grid spacings compared to the sizes of TCs. This study conducted simplified simulations of TCs using a model with much smaller spacing between grid points (i.e., high-resolution) that is able to simulate complex small-scale processes within the storms that global climate models can not. Different model simulations with warmer or cooler atmospheres and SSTs were compared. With warmer temperatures, the high-resolution simulations resulted in similar large increases in TC inner region (near the eyewall) rainfall as found in low-resolution climate models. Changes in rainfall in the outer rainbands with warming were smaller.

1. Introduction

Tropical cyclone (TC) precipitation rates are expected to increase due to anthropogenic climate change (Knutson et al., 2020), worsening the hazards associated with TC landfalls (Gori et al., 2022). Attribution studies have concluded that anthropogenic climate change has already increased precipitation from selected individual TCs (e.g., Patricola & Wehner, 2018; Reed et al., 2020, 2021; Risser & Wehner, 2017) and for the entire 2020 North Atlantic hurricane season (Reed et al., 2022). Observational precipitation products show an increase in global mean TC precipitation rates over the past few decades (Guzman & Jiang, 2021; Shearer et al., 2022). While many previous studies demonstrate that TC precipitation should continue increasing in the future due to climate change, less work has been done looking into the convective-scale mechanisms and processes within the TCs causing these projected increases. Most climate change projections use models with grid spacings ranging from 18 to 100 km, which are too coarse to resolve TC convective structures (Knutson et al., 2015, 2020; Liu et al., 2018; Stansfield, Reed, & Zarzycki, 2020; Wright et al., 2015).

Model simulations at fine enough grid spacing to switch off convective parameterizations (i.e., grid spacing around or less than 4 km) are required to study the details of TC structure. Previous research using this type of

model has focused on TC genesis and intensification processes (Davis, 2015; Ramsay et al., 2020; Wing et al., 2016), rainband formation (Moon & Nolan, 2015; Wang, 2009), and storm size (Hill & Lackmann, 2009; Martinez et al., 2020). Recently, Xi et al. (2023) studied the relationship between TC intensity and precipitation in idealized Weather Research and Forecasting (WRF) simulations with 3 km grid spacing and different domain-constant sea surface temperatures (SSTs). They found that TC inner core (IC) precipitation is highly correlated with TC intensity and increases at about 9% per K increase in SST, while outer rainband precipitation is only correlated with intensity for intensifying storms or those staying at constant intensity. Multiple modeling and observational studies have documented the relationship between SSTs, TC intensity, and TC precipitation (Kim et al., 2021; Lavender & McBride, 2021; Rios Gaona et al., 2018; Stansfield & Reed, 2023). Two recent studies found that the response of TC precipitation to climate warming is mostly controlled by the increase in atmospheric moisture, not increases in TC intensity (Kim et al., 2022; Stansfield & Reed, 2021).

The ICs and outer rainbands (OR) of TCs have different properties and characteristics. The TC IC contains the eyewall, a quasi-circular region of intense upward vertical velocities and often the highest precipitation rates, and inner rainbands. Inner rainbands typically consist of stronger convective cells on the upwind side and more stratiform regions on the downwind side (Hence & Houze, 2008). The vertical extent of the rainband deep convection does not reach as high in the troposphere as the eyewall convection (Hence & Houze, 2012). Studies of inner rainbands often split them up into principal, stationary rainbands and secondary rainbands that are more transient, but for our purposes, we will analyze them all together because they have similar convective structures and are both part of the IC of the storm (Houze, 2010). As the inner rainbands spiral out from the TC center, they tend to be made up of higher percentages of convective regions as distance from the center increases (Hence & Houze, 2012). Outer rainbands are further away from the intense storm eyewall and are more influenced by the large-scale environment. The outer storm environment contains higher Convective Available Potential Energy (CAPE) than the IC, and the OR are more like non-TC buoyant tropical deep convection (Houze, 2010). Outer rainbands tend to consist of distinct, isolated cores of deep convection with less stratiform regions than the IC (Hence & Houze, 2012). See Figure 30 in Houze (2010) for a schematic of a top-down view of reflectivity structures in a TC eyewall and inner and OR.

The formation and maintenance of TC OR can impact the storm's intensity and IC precipitation. Using idealized model simulations, Hill and Lackmann (2009) found that more moist environments favored larger TCs with more precipitation in the OR. Despite the increase in precipitation in the ORs, their simulations with more moisture in the environment did not have heavier precipitation in the eyewall. Wang (2009) and Li and Wang (2012) found that more active OR limited the intensity of TCs in their simulations, which could impact the precipitation rates in the IC. Observational studies suggest that OR can intercept some of the warm, moist air flowing radially inward toward the IC and replace it with cooler, drier air from downdrafts, thus limiting precipitation in the IC (Barnes et al., 1983; Cione et al., 2000). Stovern and Ritchie (2016) examined the response of TC precipitation and convection to various initial atmospheric temperature profiles while keeping the relative humidity profile and SST the same. They found that the simulation with the coolest temperature profile developed more outer rainband activity due to higher initial surface fluxes into the atmosphere. While the CAPE and specific humidity profiles were initially less conducive for convection than the simulations with the warmer temperature profiles, the initial strong surface fluxes developed a broader area of radial inflow that provided surface convergence to initiate convection further away from the TC center. The warmest simulation had the highest precipitation rates in the TC IC, and the coolest simulation had a more expansive precipitation field with less intense precipitation in the IC. This study shows that while a warmer atmosphere may be more moist and have initially higher CAPE, a lifting mechanism in the TC outer region is needed to generate OR, which is consistent with Li and Wang (2012).

While significant progress has been made toward understanding the formation and structure of the TC IC and OR, not many studies have focused on the partitioning of precipitation between these two regions and how that partitioning is impacted by TC characteristics such as intensity, size, and translation speed or by climate change. Shifts in the location within a TC that the heaviest precipitation accumulations occur could impact how forecasters, emergency managers, and the public prepare for future TC landfalls. The objectives of this paper are to (a) document how TC precipitation in the IC and OR in convection-permitting idealized model simulations respond to SST warming and (b) understand how changes in three-dimensional convective structures and microphysical properties within TCs contribute to these precipitation changes. The paper is organized into a Methods section that explains the model set up and analysis methods, a Results section that presents our main findings, and a

Conclusions section that summarizes the key results, discusses implications of the work, and suggests directions for future work.

2. Methods

2.1. Model Simulations

The Advanced Research WRF model, version 4.1.3 (Skamarock et al., 2019), is used to run the simulations for this study. The simulations are modified from the TC idealized test case (em_tropical_cyclone), which has doubly periodic boundaries in both the x and y dimensions and constant Coriolis forcing (i.e., an "f-plane") equivalent to f at 20°N. The WRF set-up has an outer domain with 15 km grid spacing that spans 6,000 km in the x and y dimensions, a middle nest with 5 km grid spacing that spans 2,000 km in the x and y dimensions, and an inner nest with 1.67 km grid spacing that spans about 850 km in the x and y dimensions. Only output from the inner nest is analyzed. Fierro et al. (2009) noted large improvements in the kinematic and microphysical structures of Hurricane Rita (2005) when moving from 5 to 1 km grid spacing in an older version of WRF. The inner two nests are vortex-following. There are 60 model levels in the vertical dimension, and the model top goes up to 25 km. We use the following physics parameterization schemes: Thompson aerosol-aware microphysics (Thompson & Eidhammer, 2014), MYNN2 planetary boundary layer (Nakanishi & Niino, 2006), Rapid Radiative Transfer Model for GCMs for longwave and shortwave radiation (Iacono et al., 2008), and revised MM5 surface layer (Jiménez et al., 2012). There is no land surface scheme since these simulations contain no land. The lower boundary of the model simulations is an ocean surface with a specified SST that is constant over the entire domain and remains the same throughout the integration of the simulations. The cumulus parameterization scheme is turned off for the inner nest and is set to the New Tiedtke scheme (Zhang & Wang, 2017) in the middle and outer domains. Additionally, modified surface bulk drag and enthalpy coefficients, calculated using the Garratt formulation, that are recommended based on recent TC research are used (isftcflx = 2 in the WRF namelist). Vertical velocity damping is turned on to maintain numerical stability (w_damping = 1 in the namelist), using the default vertical range for damping of 5 km from the model top.

A previous study involving idealized TC modeling found that TCs that do not move around during a simulation do not experience asymmetrical frictional convergence associated with the low-level environmental flow and therefore tend to lack convection in the TC outer region compared to observed TCs (Martinez et al., 2020). Following the lead of Martinez et al. (2020) and Nolan (2011), we add a uniform horizontal background wind of 3 m/s throughout the troposphere in the x dimension in our simulations to prevent the TCs from remaining in one spot in the middle of the WRF domains. This is done through a method known as "point-downscaling" by adding an extra term to the meridional momentum equation that accounts for the pressure force needed to balance the wind shear if a temperature gradient did exist (Nolan, 2011; Onderlinde & Nolan, 2017). This allows a background wind to exist without a surface temperature gradient and is implemented through the "pert_coriolis" option in the WRF namelist. All of the WRF settings and schemes are chosen based on recommendations for TC simulations from the WRF manual, previous research results (e.g., Brown et al., 2016), and advice from researchers who have previous experience with TC modeling in WRF. The simulations are run for 8 days total, and output in the inner domain is saved at 15 min intervals. The first 24 hr of the simulations are not analyzed to allow for spin-up of the TCs. The only difference between the four simulations are the SSTs, which are set to 298, 300, 302, and 304 K in the four different simulations.

To calculate vertical profiles of temperature and moisture to initialize the WRF TC simulations, 100 day radiative convective equilibrium (RCE) simulations are run on small doubly periodic domains (101 by 101 gridpoints with 3 km grid spacing). The same physics parameterization schemes used for the inner nest of the full TC simulations are also used for the RCE simulations. The simulations have 40 vertical levels and extend up to 25 km in height. There is a small Coriolis force equal to 2.5×10^{-5} s^{-1}, and random low-level temperature perturbations are added to initiate convection. Four of these RCE simulations are run with domain and time constant SSTs of 298, 300, 302, and 304 K. The domain-mean potential temperature and specific humidity profiles from the last 30 days of the simulations (Figure 1) are used as the initial profiles for the TC simulations. These vertical profiles are qualitatively similar to the default sounding used in the idealized TC test case (Jordan, 1958), shown as the black dashed line in Figure 1. Similar methods have been used to create initialization profiles for idealized TCs in previous studies (Ramsay et al., 2020; Xi et al., 2023). All TC simulations are initialized with the same weak, axisymmetic vortex based on Rotunno and Emanuel (1987) with the default settings in the WRF TC test case. To

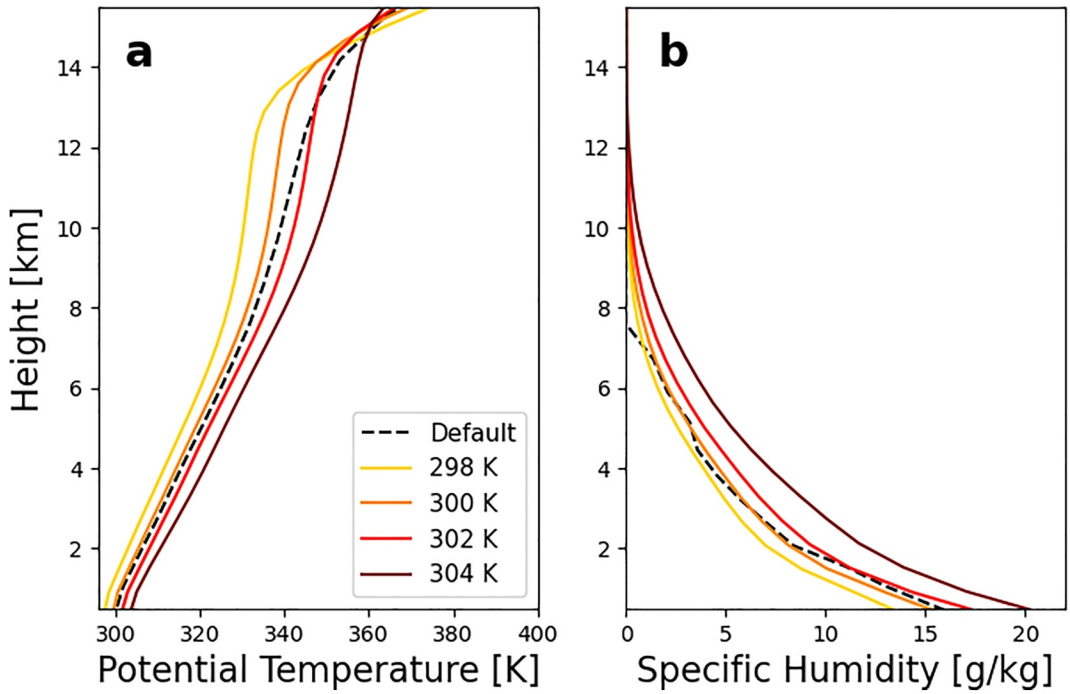

Figure 1. Vertical profiles of (a) potential temperature [K] and (b) specific humidity [g/kg] for the (black dashed line) default input sounding for the idealized Weather Research and Forecasting tropical cyclone test case that is derived from observations (Jordan, 1958) and domain mean of the last 30 days of radiative convective equilibrium simulations with SSTs of (yellow) 298 (orange) 300 (red) 302, and (dark red) 304 K.

test the robustness of our results, we created a few ensembles of the 300 K simulation by adding small random perturbations to the initial specific humidity field in the boundary layer, following Martinez et al. (2020). These ensemble simulations are discussed in the Supplemental Material (Text S1 in Supporting Information S1), but ultimately the results suggest that our main conclusions about changes in the TC precipitation with SST warming are not highly sensitive to small perturbations in the initial conditions of the simulations.

2.2. TC Size Calculations and Storm Mode Classification Algorithm

To demonstrate that the TCs in our simulations look realistic, Figures 2a–2d shows simulated reflectivity at a height of 2 km 48 hr after model initialization. All four TCs have reasonable reflectivity patterns, including small areas of very high reflectivity near the storm center and rainbands spiraling out from the center. Before analyzing changes in TC precipitation with SST warming between the outer region and IC of the storm, the boundaries between these regions must be defined. Previous studies tend to either define the IC radius using the radius of maximum wind speed (Wang, 2009), the radius of maximum precipitation (Guzman & Jiang, 2021), or a fixed threshold of around 100 km (Wei et al., 2022). We wanted to use a dynamic threshold, since TC size can vary over time and by storm, so this study's definition of the radius of the TC IC is two times the radius of the maximum azimuthal wind speed. As an example, this radius is plotted as the magenta circle in Figure 2. All points from this radius to the center of the storm are considered the IC of the storm. We tried to define the IC radius using the azimuthal mean profile of precipitation, but because of the high resolution of these simulations, the profiles were noisy and therefore the radius of the maximum precipitation changed very frequently. The radius of the maximum azimuthal wind speed was more stable over time. The outer radius of the TC is defined as the radius of the 8 m/s azimuthal mean wind speed, which is another radius commonly used to define the outer size of a TC (Chavas et al., 2017; Schenkel et al., 2017; Stansfield, Reed, Zarzycki, Ullrich, & Chavas, 2020). As an example, this radius is plotted as the black circle in Figure 2. All points between the IC radius and this radius are considered the outer region of the storm. The radii are recalculated at every output timestep since the storms' sizes change over time. A sensitivity test to the definitions of the TC IC and outer region radii thresholds is presented in the Supplemental Material in Text S2 in Supporting Information S1.

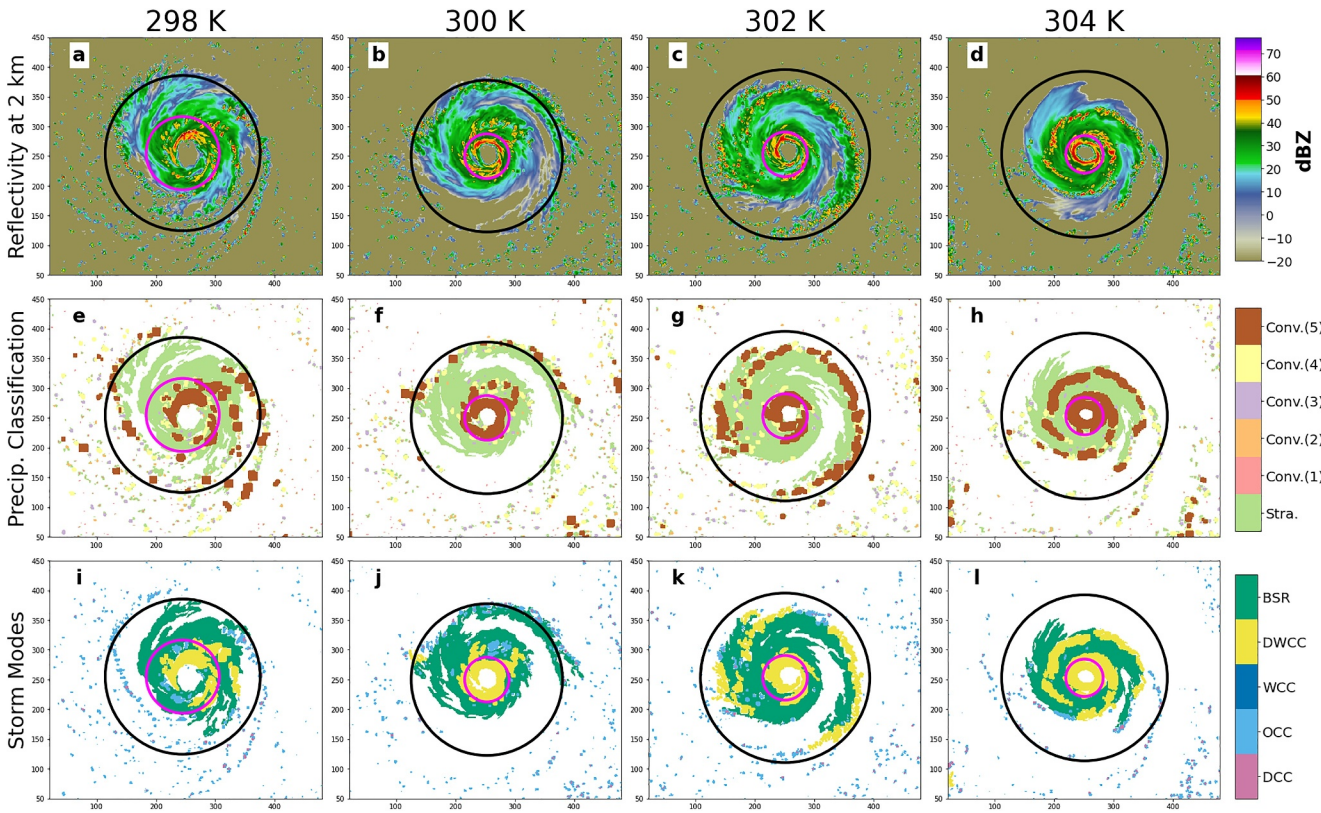

Figure 2. Snapshots of (a)–(d) 2 km simulated reflectivity [dBZ] (e)–(h) convective and stratiform precipitation classifications, and (i–l) Storm Mode classifications at 48 hr after model initialization with domain-constant SSTs of (a,e,f) 298 (b,f,j) 300 (c,g,k) 302, and (d,h,l) 304 K. The magenta circle in each panel indicates two times the radius of maximum wind, defining the outer radius of the inner core, and the black circle indicates the radius of the 8 m/s azimuthal wind speed, defining the outer radius of the outer region of the storm. Explanations for the storm mode abbreviations can be found in Section 2.2.

Figures 2e–2h shows the breakdown of the precipitation into stratiform and convective types 48 hr after model initialization. Areas of reflectivity output are classified based on the magnitudes, heights, and widths of the values, using methodology and parameter values from Steiner et al. (1995). The TC precipitation classifications look as expected based on previous work, with convective areas surrounding the centers of the TCs (i.e., the eyewalls), stratiform areas wrapping around the eyewalls, and relatively small convective cores surrounded by stratiform areas in the outer regions (Hence & Houze, 2012; Houze, 2010). Figures 2i–2l shows the TCs at the same snapshot in time but classified into different storm modes. Houze et al. (2007) first defined the storm mode categories to study the storm climatology in the Indian subcontinent using the first spaceborne precipitation radar on the Tropical Rainfall Measuring Mission (TRMM) satellite. The storm mode categories have since been developed further and are defined as: (a) deep convective cores (DCCs)—30 dBZ echo volumes ≥8 km in altitude; (b) wide convective cores (WCCs)—30 dBZ echo volumes ≥800 km^2 in horizontal area; (c) deep and wide convective cores (DWCCs)—storms that satisfy both the DCC and WCC criteria; (d) ordinary convective cores (OCCs) - 30 dBZ echo volumes that meet neither the deep or wide thresholds (likely convection during intensifying or decaying stages); and (e) broad stratiform regions (BSRs)—contiguous stratiform rain area ≥ 40,000 km^2 in horizontal area (H. Yu, 2022). Numerous studies have used these storm modes to investigate the nature of extreme storms around the world (Houze et al., 2015; K. L. Rasmussen & Houze, 2011; K. L. Rasmussen & Houze, 2016), but to the authors' knowledge, this study is the first to apply this classification to TCs. One small modification made to the classification algorithm was defining the minimum area of BSRs as ≥ 30,000 km^2 instead of the original value of ≥40,000 km^2, which is defined as a moderate threshold in Houze et al. (2015).

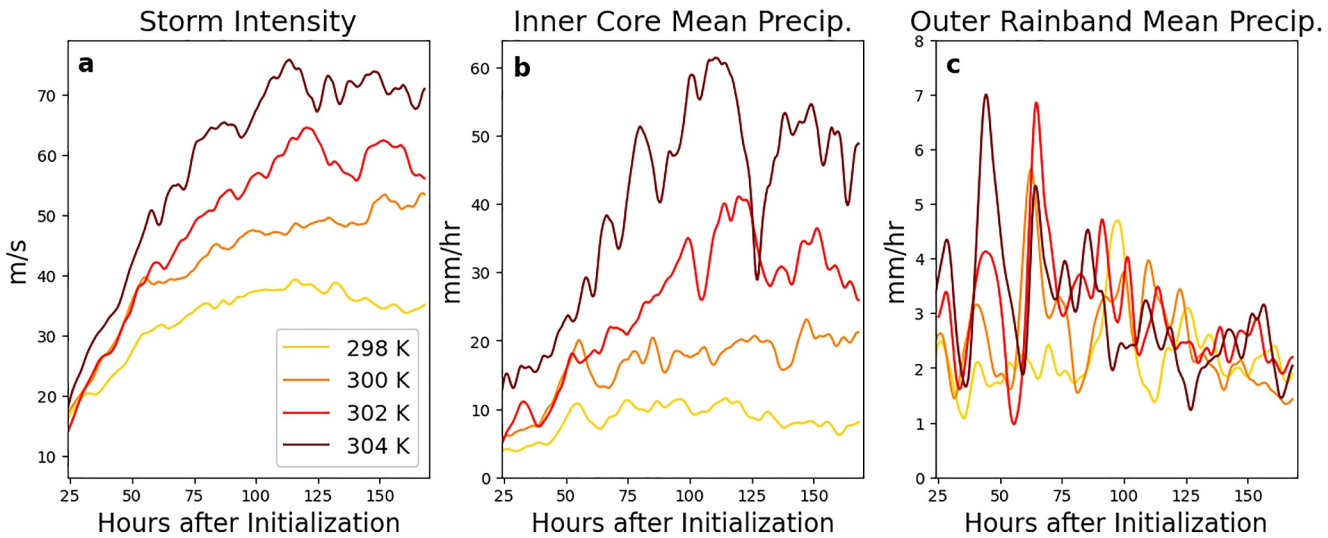

Figure 3. Time series of (a) tropical cyclone (TC) intensity in m/s, measured by the maximum 10 m azimuthal-mean wind speed, (b) mean precipitation in mm/hr in the TC inner core, and (c) mean precipitation in mm/hr in the TC outer rainbands in the 298, 300, 302, and 304 K simulations. The *x*-axis shows the hours after model initialization. For plotting purposes, all time series are smoothed using a 12 hr low-pass Lanczos filter.

3. Results

3.1. TC Intensity and Precipitation Response to Warming

To begin, the simulated TC intensities and precipitation in the ICs and OR are compared. Tropical cyclone intensity at each timestep is calculated as the maximum azimuthal-mean 10 m wind speed. Both the time mean and lifetime maximum TC intensities increase with warming SSTs (Figure 3a). The lifetime maximum TC intensities are 41.2, 57.8, 69.1, and 83.1 m/s for the 298, 300, 302, and 304 K simulations, respectively. Note that the values of TC intensity in Figure 3a do not reach these values because the time series are smoothed using a 12 hr low-pass Lanczos filter to minimize high-frequency variability for easier visual interpretation of the plots. Higher intensities with warmer SSTs are consistent with theoretical expectations of the relationship between SST and TC intensity (Emanuel, 1999) and with previous studies of TCs in idealized simulations (Xi et al., 2023). The time and spatial mean potential intensity (Emanuel, 1999; Gilford, 2020) increases from 67.8 m/s in the 298 K simulation to 79.5 m/s in the 304 K simulation. We note here that the TC intensity changes with SST in these simulations are much larger than observed TC intensity changes since the beginning of the satellite record (Kossin et al., 2013; Sobel et al., 2016). This is partially because TCs in these WRF simulations are in ideal conditions for TCs (e.g., warm constant SSTs, low vertical wind shear) and partially because of the large range of SSTs in our simulations (298–304 K). The range of SSTs in our simulations is much larger than the observed global mean SST changes in the historical record (Xu et al., 2021). We chose to use this large SST range to maximize the chance of having large differences in the TC properties, which facilitates analysis of the processes causing these differences. Because of the significant SST and TC intensity increases in these simulations, they create signals in TC precipitation that are much larger than what we can expect to see in the real world as global SSTs warm, at least on the timescales of decades to centuries.

The IC precipitation increases with warming SST (Figure 3b and Table 1). Mean OR precipitation increases with warmer SST when comparing the 298, 300, and 302 K simulations but not between the 302 and 304 K simulations (Figure 3c and Table 1). The OR precipitation does not increase as much as the IC precipitation. The mean percent increase of the mean IC precipitation is 35.1% per K compared to 5.5% per K for the mean OR precipitation. The mean precipitable water in the IC and OR also increase with SST at about 8.9% per K and 9.4% per K, respectively (Table 1). The IC precipitation increases more quickly with warmer SSTs than IC precipitable water. This could be caused by a few different changes in the IC, such as stronger dynamical forcing (i.e., stronger upward motion shown in Table 1), increased precipitation efficiency (PE), or both. To examine another metric of TC precipitation, we summed all precipitation in the TC IC and OR at each timestep, calculated the time mean of this accumulated precipitation over Days 2–7 of each simulation, and then multiplied by the number of hours to

Table 1
Time Mean Statistics for the Tropical Cyclone Inner Cores and Outer Rainbands

	298 K	300 K	302 K	304 K
IC Mean Precipitation [mm hr^{-1}]	8.5	16.9*	25.7*	41.2*
OR Mean Precipitation [mm hr^{-1}]	2.2	2.6*	3.0*	3.0
IC Accumulated Precipitation [mm]	1.1×10^7	1.4×10^7*	1.5×10^7	1.7×10^7*
OR Accumulated Precipitation [mm]	1.5×10^7	1.3×10^7	1.6×10^7*	1.7×10^7
IC Mean Precipitable Water [kg m^{-2}]	46.8	53.5*	63.5*	76.3*
OR Mean Precipitable Water [kg m^{-2}]	40.1	46.8*	55.1*	67.1*
IC Mean Upward Vertical Velocity [m s^{-1}]	0.55	0.80*	1.08*	1.57*
OR Mean Upward Vertical Velocity [m s^{-1}]	0.22	0.24*	0.27*	0.32*
IC Max. Vertical Velocity [m s^{-1}]	17.4	16.6	17.7*	17.6
OR Max. Vertical Velocity [m s^{-1}]	21.6	23.8*	25.4*	27.8*
IC Mean Melting Level [km]	4.1	4.6*	5.3*	6.0*
OR Mean Melting Level [km]	3.7	4.1*	4.7*	5.3*
Mean Cloud Base Height [km]	2.4	2.3*	2.1*	1.8*
IC Radius [km]	91.9	73.5*	61.9*	52.4*
OR Radius [km]	341.5	353.1	362.1	360.4

Note. All time means are calculated over Days 2–7 of the simulations. Asterisks next to the 300, 302, and 304 K values indicate that the null hypothesis is rejected at the 1% level using a Mann-Whitney U test with an alternative hypothesis that the distribution from the warmer simulation is greater than the distribution from the 2 K cooler simulation, except for cloud base height and IC radius where the alternative is that the warmer simulation distribution is lower.

convert to units of mm. The accumulated precipitation increases in these simulations in the TC IC with warmer SST and also increases in the OR, except when comparing the 300 K simulation to the 298 K simulation (Table 1). Asterisks in Table 1 indicate when the distribution of that variable is statistically significantly greater at the 1% level than the distribution from the simulation that is 2 K cooler, tested using a Mann-Whitney U test. Given the observed relationship between surface equivalent potential temperature and extreme precipitation in the tropics (Song et al., 2022), the time mean equivalent potential temperature at 2 m above the surface within the TC area was calculated for each simulation. The equivalent potential temperature increases monotonically from 341.9 K in the 298 K simulation to 372.7 K in the 304 K simulation, with a mean increase of about 5 K per 1 K increase in SST, which is larger than the increase in mean 2 m air temperature of about 1 K per 1 K increase in SST (not shown). The mean TC IC precipitation is highly correlated with the mean equivalent potential temperature at each timestep (Spearman's Rank correlation coefficient of 0.87).

In concert with intensification of the maximum azimuthal-mean wind speed of a TC (a measure of its primary circulation), the secondary "in-up-out" circulation also intensifies. This is shown in Figure 4, which shows time and azimuthal mean vertical velocities in the shaded contours and radial velocities in the line contours for each simulation. All of the panels show the strongest upward motion in the eyewall of the TCs, about 20–70 km from the storm center. Outside of the eyewall, there is very weak vertical motion, with some subsidence. There is flow into the center of the TCs near the surface up to about 2 km in height, and in the upper levels around 10–15 km, there is flow away from the storm center. All of these features are expected based on observations and our theoretical understanding of the TC circulation (Emanuel, 1991). As SST increases, the mean upward vertical velocities in the IC and OR increase (Table 1), and the radial inflow and outflow increase in magnitude as well (Figure 4). The outflow also appears to move higher with SST warming, suggesting a vertical deepening of the TC circulation. This will be discussed more in Section 3.3.

Stronger upward motion in saturated environments typically leads to higher precipitation rates (Doswell et al., 1996). Figure S3 in Supporting Information S1 shows a time series of maximum precipitation rates in the IC and OR. Similar to mean precipitation, maximum precipitation increases markedly in the IC but does not show a large change in the OR. However, the magnitudes of maximum precipitation in the IC and OR are fairly similar, suggesting that both the IC and OR contain strong updrafts and convective precipitation processes. Table 1 shows

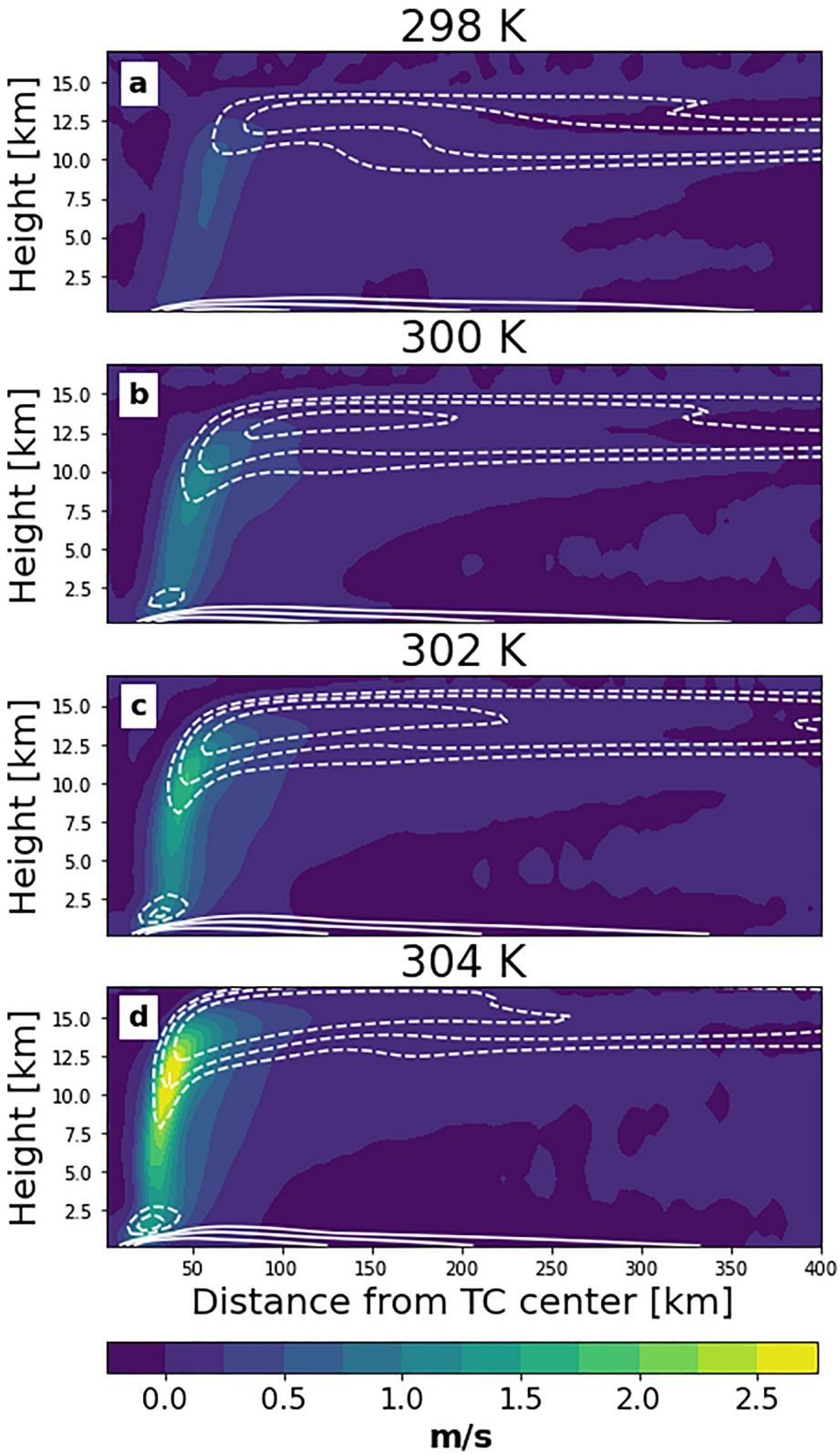

Figure 4. Time mean and azimuthal mean vertical profiles of vertical wind speed in m/s (shading) and radial wind speed in m/s (white line contours) for the (a) 298, (b) 300, (c) 302, and (d) 304 K simulations. Solid line contours indicate motion toward the center of the tropical cyclone (TC) while dashed contours indicate motion away from the center. The line contours shown are −10, −5, −2.5, 2.5, 5, and 10 m/s. The *y* axis shows height in km above the surface, and the *x* axis shows the distance from the TC center in km.

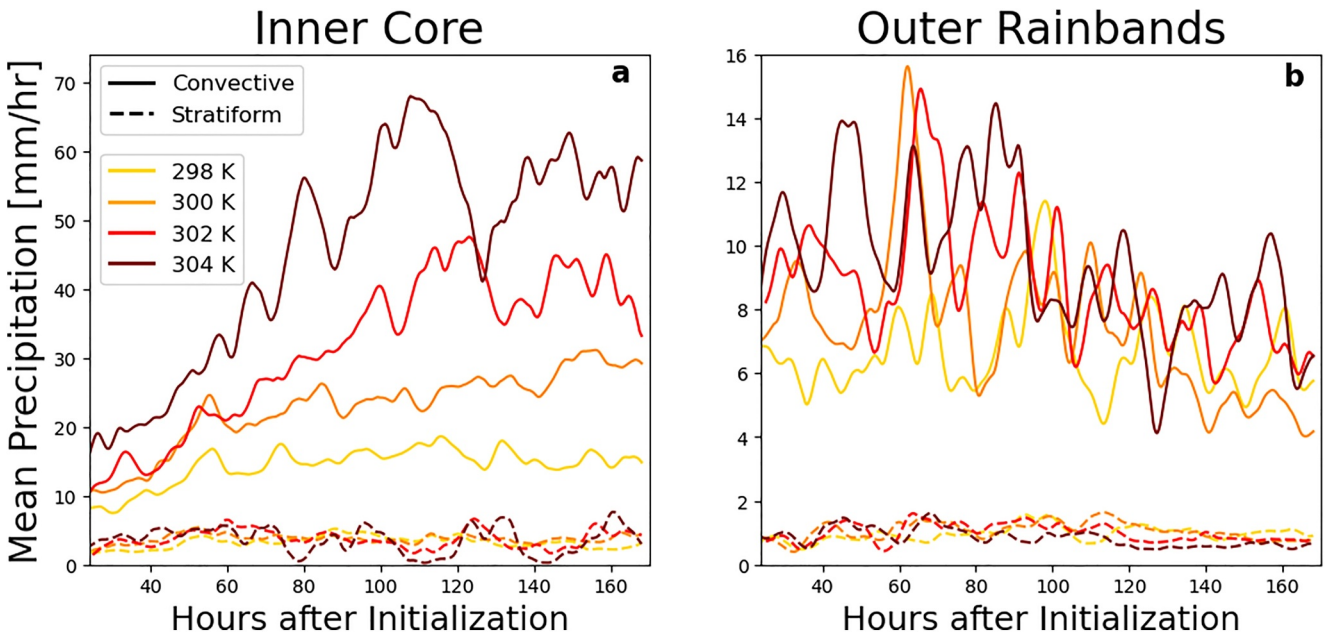

Figure 5. Time series of mean precipitation in mm/hr in the tropical cyclone (a) inner core and (b) outer rainbands from convective (solid lines) and stratiform (dashed lines) regions in the 298, 300, 302, and 304 K simulations. The *x*-axis shows the hours after model initialization. For plotting purposes, the time series are smoothed using a 12 hr low-pass Lanczos filter.

the time mean maximum vertical velocity in the TC IC and OR. The maximum vertical velocity increases steadily with warmer SST in the OR, while for the TC IC, there is not a monotonic trend as SST increases. It has been suggested in previous studies that convection in the OR is more "traditionally convective" and related to CAPE (Houze, 2010) but that convection in the IC is driven more by the TC circulation itself and is not strongly related to CAPE/buoyancy (Smith & Montgomery, 2022). CAPE increases with warmer SSTs in our simulations (not shown), which explains why the maximum vertical velocity in the OR increases.

Typically the highest precipitation rates in TCs come from convective processes. Figure 5 shows the temporal evolution of the mean precipitation in the (a) IC and (b) OR, split into convective (solid lines) and stratiform (dashed lines) regions. In the IC, most of the precipitation comes from convective regions and most of the increase in mean IC precipitation with SST warming seen in Figure 3 comes from convective regions. The stratiform precipitation amounts in the IC do not vary as much with SST, with time mean values ranging from 3.3 mm/hr in the 298 K simulation to 3.8 mm/hr in the 302 K simulation. In the OR (Figure 5b), the convection areas produce more precipitation as well. The increase in convective precipitation with SST warming is less obvious than in the IC, but the time means do increase monotonically from 6.8 mm/hr in the 298 K simulation to 9.6 mm/hr in the 304 K simulation. The time mean stratiform precipitation in the OR is smaller and changes non-monotonically with warming, ranging from 0.8 mm/hr in the 304 K simulation to 1.1 mm/hr in the 300 K simulation. The increase in precipitation from convective regions in the IC and OR can come from increases in precipitation rates, increases in the size of the convective regions, or both. These possibilities will be discussed in the following two sections.

3.2. Changes in Storm Structures With Warming

Before examining changes in storm modes in the TCs with SST warming, we first look at the percentage of the IC and OR that consist of convective regions (Figure 6). This is motivated by the finding in Hence and Houze (2012) that higher SSTs increase the fraction of convective precipitation in all regions of TCs as seen in TRMM radar reflectivity data from 1998 to 2007. We examine the differences in the percent of gridpoints in the IC and outer region since the TCs are different sizes throughout the simulations. The percent of gridpoints covered by convection in the IC (solid lines in Figure 6) increases with warming SSTs, while the size of the IC gets smaller (Table 1). The difference in convective area is large between the coolest and warmest simulation, with temporal means of 43.7% in the 298 K simulation and 83.8% in the 304 K simulation. This increase in the area of

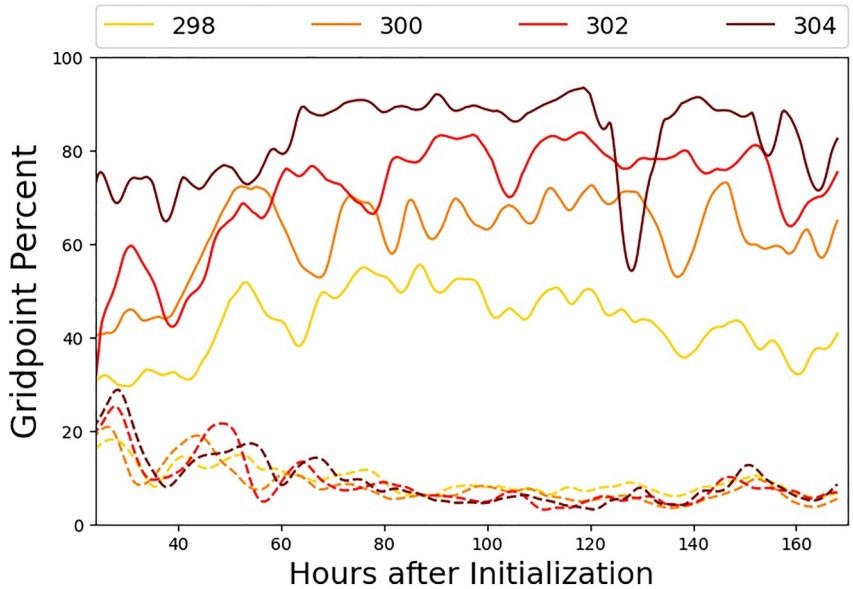

Figure 6. Time series of percentage of gridpoints covered by convective regions for the tropical cyclone inner core (solid lines) and outer rainbands (dashed lines) in the 298, 300, 302, and 304 K simulations. Time series are smoothed using a 12 hr low-pass Lanczos filter.

convection in the IC accounts for at least part of the increase in mean convective precipitation displayed in Figure 5a. The Spearman's rank correlations between the percent of convective area in the IC and the mean IC precipitation are 0.90 for 298 K, 0.71 for 300 K, 0.69 for 302 K, and 0.55 for 304 K (all significant at the 1% level). While the correlation is smaller for the 304 K simulation for the full period of the simulation, the correlation is closer to 0.85 for the first 2–3 days (after the 24 hr spin-up period) when the TC is intensifying. After this intensification period, the correlation is lower, which we hypothesize is due to the persistent high percentages (i.e., above 90%) of IC area occupied by convective regions in the 304 K simulation (Figures 2h and 6). Although convective regions occupy less area in the OR than stratiform (dashed lines in Figure 6), they still contribute most of the precipitation in the outer region (Figure 5b). There is minimal difference in the percent of convective gridpoints in the outer regions between the different simulations with temporal means of 9.2%, 7.9%, 8.4%, and 9.0% for the 298, 300, 302, and 304 K simulations, respectively.

To explore changes in storm structure further, we further classify the convective and stratiform regions in the TCs into storm modes. The explanation for the abbreviations of the storm modes can be found in Section 2.2. First, we plot the spatial frequencies of the storm modes over the full length of the simulations (Figure S4 in Supporting Information S1), showing that DWCCs and BSRs are by far the most common modes in the TCs. DWCCs tend to occur in the IC of the storms more than the OR, while BSRs occur mostly in the transition regions between the IC and OR and outward. Ordinary convective cores, DCCs, and WCCs occur much less frequently over the TC lifetimes, so they will not be discussed here. Figure 7 shows the difference in the temporal occurrence frequencies of (a,c,e) DWCCs and (b,d,f) BSRs between the (a,b) 298 and 300 K simulations (c,d) 300 and 302 K simulations, and (e,f) 302 and 304 K simulations. DWCCs tend to increase in occurrence near the TC center and decrease outside the center with SST warming. This suggests a contraction of the convective regions toward the center of the storms, in line with the decrease in the mean radii of the IC with warming (Table 1). With warming, the BSR frequencies decrease, mostly in the outer regions of the storms. The change in BSR frequency is larger between the 298 and 300 K simulations compared to the other pairs of simulations. Changes in stratiform regions have a much smaller impact on the changes in precipitation with warming in both the IC and outer regions, as shown by the much smaller contribution to total precipitation from stratiform areas compared to convective areas in Figure 5.

3.3. Changes in Microphysics With Warming

To complement the analysis of TC precipitation and structure changes, we next examine changes in microphysics through changes in mixing ratios of various hydrometeors and cloud liquid and ice in Figure 8. Mean mixing

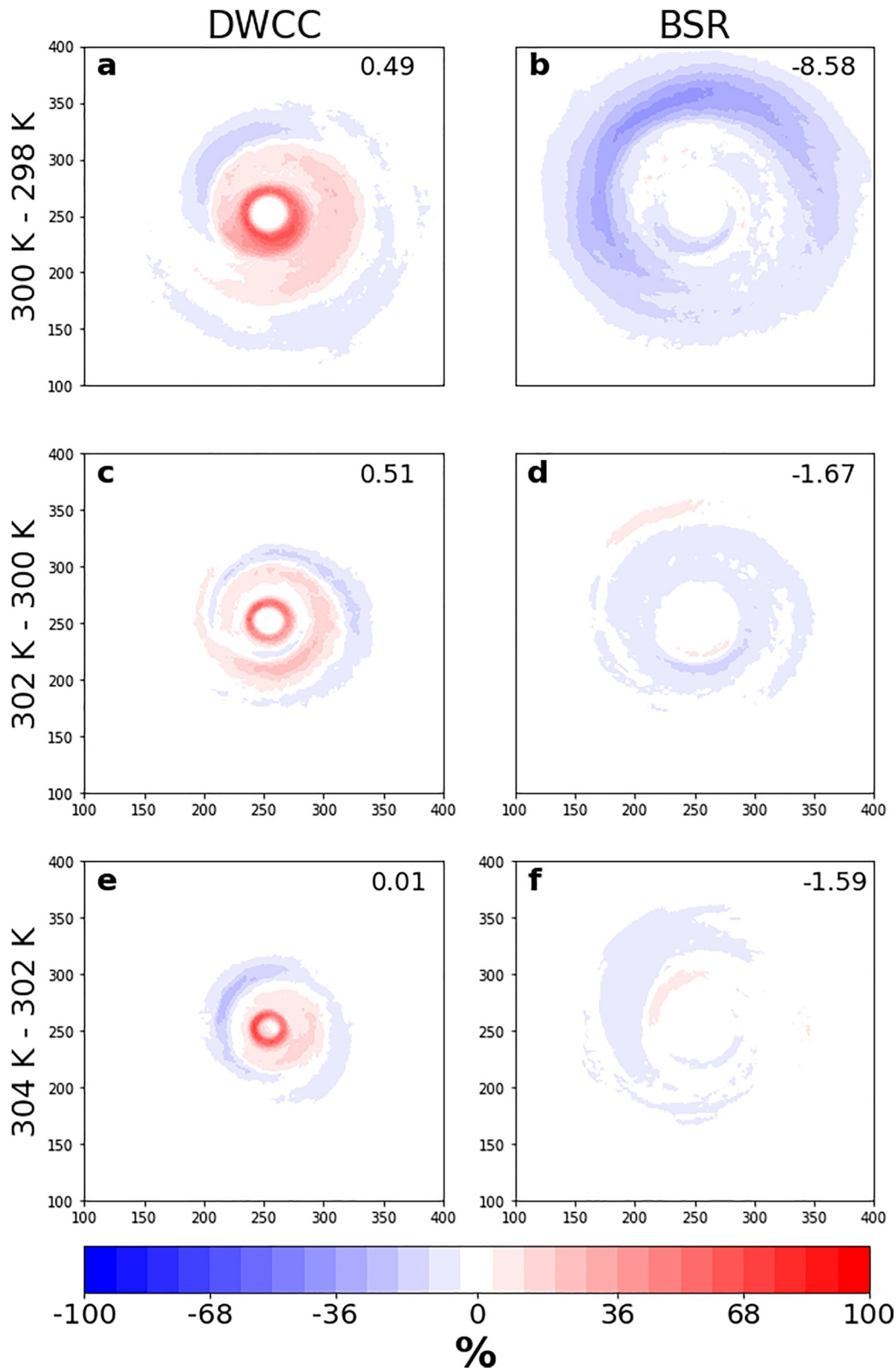

Figure 7. Change in occurrence frequency [%] of (a,c,e) DWCCs and (b,d,f) BSRs for (a), (b) the 300 K simulation minus the 298 K simulation (c), (d) the 302 K simulation minus the 300 K simulation, and (e), (f) the 304 K simulation minus the 302 K simulation. Numbers in the top right show the mean value over the whole spatial domain.

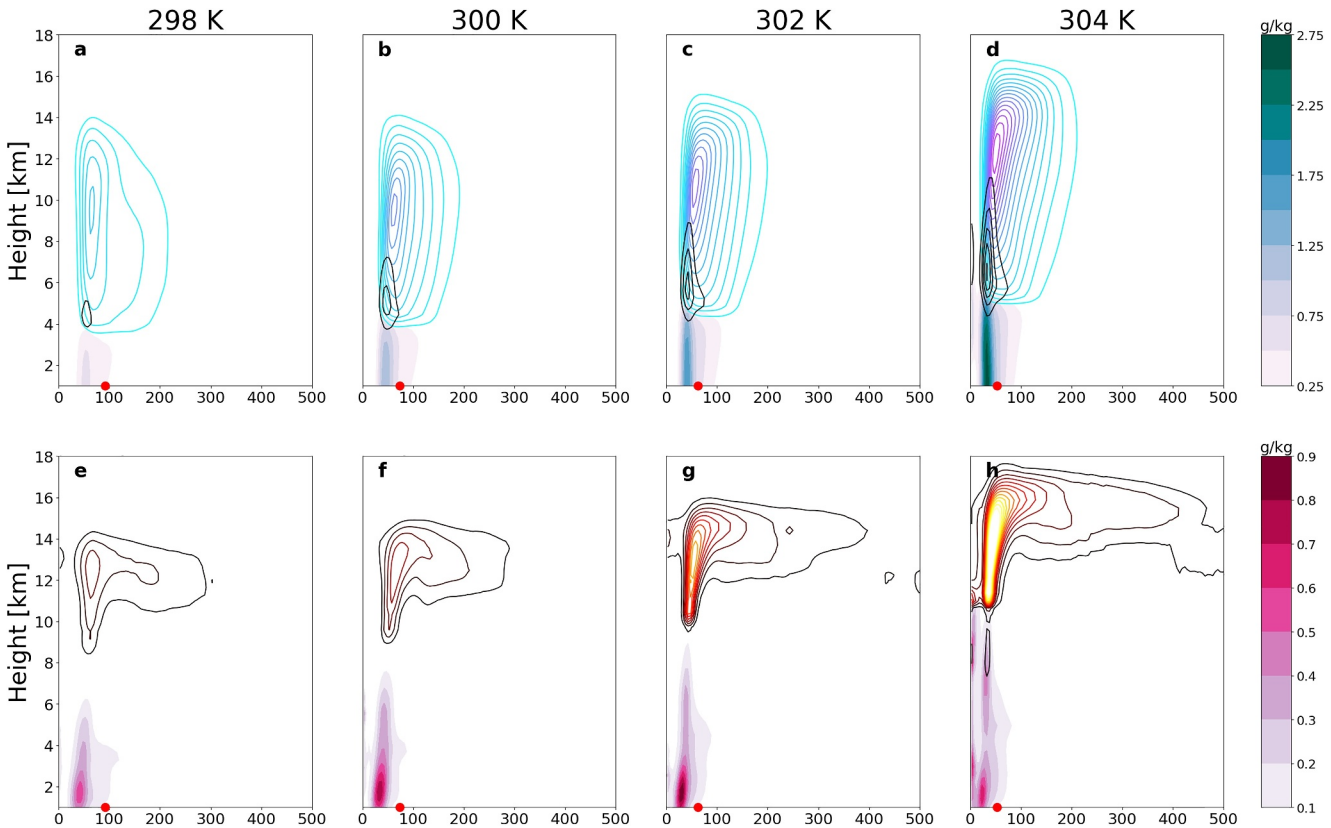

Figure 8. Time and azimuthal mean mixing ratios [g/kg] of (a)–(d) rain (filled contours), snow (colored contour lines), and graupel (black contour lines) and (e)–(h) cloud liquid (filled contours) and ice (contour lines) for the (a), (e) 298 K (b), (f) 300 K (c), (g) 302 K, and (d), (h) 304 K simulations. For a-d, the colored line contours start at 0.25 g/kg and go up to 4.75 in 0.25 g/kg increments, and the black contours start at 0.2 g/kg and go up to 3.0 g/kg in 0.2 g/kg increments. For e-h, the contour lines start at 1.0×10^{-3} g/kg and go up to 0.015 g/kg in 1.0×10^{-3} g/kg increments. Time means are taken over Days 2–7 of the simulations.

ratios of all hydrometeors increase with warming (Figures 8a–8d). The maximum values of rain (filled contours) not only increase with warming but also contract toward the TC centers, consistent with the contraction of the IC sizes with warming (Table 1) and more frequent occurrences of DWCCs in the IC with warming (Figures 7a–7 c and 7e). In line with observations, there is evidence of cold-phase precipitation formation (i.e., graupel and snow) in the IC of the TCs (Houze, 2010). The snow (colored line contours) mixing ratio maxima increases and moves higher in the atmosphere with warming. Similarly, the graupel (black line contours) mixing ratios concentrate more toward the TC centers, where the strongest updrafts are found in the eyewalls, and extend higher into the atmosphere with warming, suggesting higher lofting of graupel by stronger updrafts (Table 1). The mean height of the melting layer (height of the 0°C isotherm) increases as SST increases (Table 1). This is in agreement with Hence and Houze (2012) who analyzed TRMM radar reflectivity data and found that higher SSTs shift the melting layer signature higher in the atmosphere. Mean cloud base heights become lower in the atmosphere with warming in these simulations (Table 1), which in combination with a rising melting layer creates a larger volume for warm rain processes. The mean echo top height (defined as the maximum height of a 20 dBZ reflectivity value) rises with warming in both the IC and outer region (Table S1 in Supporting Information S1), demonstrating the increasing vertical extent of the TC circulations.

Figures 8e–8h shows the mixing ratios of cloud liquid (filled contours) and cloud ice (line contours). The amount of cloud ice increases with SST warming and moves upward, suggesting a thickening and rising of the TC anvil clouds. The cloud liquid mixing ratios extend higher vertically and decrease in maximum magnitude between the 302 and 304 K simulations. This could indicate an increase in PE with warming, as condensed liquid remains in the atmosphere for a shorter time before falling as rain. An increase in PE was found with warming in small-domain RCE simulations by Lutsko and Cronin (2018). Using a simple definition of PE (the quotient of precipitation and precipitable water, excluding any gridpoints where precipitation is 0 mm/hr) that has been used for

real world TCs before (Brauer et al., 2020), we calculated the maximum PE and mean PE in the IC and outer region at each timestep during Days 2–7 of the simulations and then found the mean over all timesteps (Table S1 in Supporting Information S1). Both the maximum and mean PE increase with warming SST in the TC IC. In the OR, the maximum PE decreases with warming SST while the mean PE remains about the same, except when comparing the 302 and 304 K simulations. This provides an additional explanation for why there are large increases in IC precipitation with SST warming and smaller increases in outer rainband precipitation. Precipitation efficiency is a very complex process; therefore, it is difficult to point to one reason for PE changes. With warmer SST in our simulations, the volume available for warm precipitation production processes increases due to the lower cloud base heights and higher melting levels (Table 1). With a larger volume for these processes to occur plus higher mixing ratios of water vapor and cloud water (Figure 8), we hypothesize that there are more efficient warm rain processes, such as collision and coalescence, which increases the PE in the TC IC. It is thought that warm rain processes are very important for precipitation production in the TC IC, while cold phase precipitation production is more dominant in the OR (Hu et al., 2020; Wu et al., 2021). The dominance of different precipitation production types may explain the different response of PE to SST warming in the IC versus the OR in our simulations, but more work is required to study these processes in more detail.

4. Conclusions

This work compares idealized convection-permitting WRF simulations of TCs in doubly periodic domains with different domain-constant SSTs. The main motivation is to study the response of precipitation in the TC IC and OR to SST warming to gain an understanding of how precipitation in TCs in the real world may be impacted by climate change. Additionally, we examine changes in the three-dimensional storm structures and microphysical characteristics to understand why TC precipitation changes with warming in the model simulations. The simulations produce large increases in TC intensity and IC precipitation with SST warming. The OR precipitation also increases (except between the 302 and 304 K simulations) but at a smaller rate than the IC precipitation. In all areas of the TCs, most of the precipitation comes from convective regions as opposed to stratiform regions. The percentage of the IC occupied by deep convection greatly increases with warming, thus contributing to the large increase in precipitation, while the percentage in the TC outer region changes minimally. In the IC, DWCCs occur more frequently and closer to the TC center with warming, while the BSRs in the TC outer region occur less frequently with warming. This work demonstrates that storm mode classification works well on TCs, at least in a model, and is useful for gaining insight into what processes are changing precipitation in different regions of TCs. The vertical extent of the TC circulation deepens with warming, the melting level rises higher in the atmosphere, and the mixing ratios of all hydrometeors increase, especially in the IC, along with the precipitable water. While PE increases in most cases in the TC IC with warming, potentially due to the larger volume available for warm rain processes, the maximum PE decreases in the OR.

Interestingly, multiple recent studies have found a decreasing trend in global mean TC IC precipitation and an increasing trend in OR precipitation since 1998 using satellite precipitation products (Guzman & Jiang, 2021; Tu et al., 2021; Wei et al., 2022). Lai and Toumi (2023) found a decrease in the fraction of high thick clouds in TC ICs from 2002 to 2021, which suggests a weakening of IC convection. In contrast, both the convection-permitting model simulations in this study and global climate models simulate increases in TC IC precipitation with climate warming. We hypothesize that the decreasing trend in TC IC precipitation found in satellite data, if it is a true signal and not due to instrument continuity issues, is caused by internal variability or shifts in the climate beyond just SST warming, such as changes in atmospheric dynamics, meaning that the WRF model simulations in this paper are too idealized to simulate the observed trends. Our simulations also do not include a coupled ocean model that could lead to ocean mixing and the upwelling of cooler ocean waters to the surface (Huang et al., 2021; Kanada & Aiki, 2024), external triggers for outer rainband formation (C.-K. Yu et al., 2023), strong vertical wind shear that helps force and organize TC precipitation in the real world (Wingo & Cecil, 2010), or impacts of aerosols (Sena et al., 2024; Wang et al., 2014). Future work will involve repeating the analysis performed in this study on TCs in convection-permitting regional WRF simulations that have both historical and pseudo-global warming runs (R. Rasmussen et al., 2023). We will assess if the convective-scale TC precipitation responses to climate warming in these more realistic convection-permitting WRF runs will differ from the idealized runs analyzed in this paper.

Other possibilities to explain the discrepancy between models and observations in TC IC precipitation trends are errors in the observed trends due to the relatively coarse resolution (about 10–25 km) of the satellite precipitation

products used in the observational studies (Huffman et al., 2010, 2019), discontinuities in the satellite observational record due to satellite adjustments and instrument changes, and underestimation of very heavy precipitation rates within the TC ICs (Iguchi et al., 2009). In conclusion, this work demonstrates the need to pursue process-based understanding of small-scale, three-dimensional storm mode structures and microphysical processes in TCs, as these characteristics can greatly impact the amount of precipitation produced in different regions of the TC. This finding encourages the continued use of convection-permitting models to explore the influence of climate on TC precipitation.

Data Availability Statement

While the full output of the WRF model simulations is extremely large, all data and python scripts required to make the figures in the paper as well as the WRF namelist file are available on Zenodo (Stansfield, 2025). Anyone with interest in using the full model output is encouraged to contact the first author. WRFv4.1.3 source code can be downloaded at https://www2.mmm.ucar.edu/wrf/users/download/get_source.html.

Acknowledgments
The authors would like to thank Michael Bell and Chelsea Nam for their advice on setting up the TC simulations in WRF. Stansfield acknowledges funding support from her NSF AGS Postdoctoral Award (NSF award number 2204138). Rasmussen acknowledges funding from DOE ASR grant DE-SC0022056, NASA Grant 80NSSC22K0608, and NSF award number 2312317. The authors would like to acknowledge high-performance computing support from Cheyenne (doi:10.5065/D6RX99HX) provided by NCAR's Computational and Information Systems Laboratory, sponsored by the National Science Foundation.

References

Barnes, G., Zipser, E., Jorgensen, D., & Marks, F., Jr. (1983). Mesoscale and convective structure of a hurricane rainband. *Journal of the Atmospheric Sciences*, *40*(9), 2125–2137. https://doi.org/10.1175/1520-0469(1983)040⟨2125:MACSOA⟩2.0.CO;2

Brauer, N. S., Basara, J. B., Homeyer, C. R., McFarquhar, G. M., & Kirstetter, P. E. (2020). Quantifying precipitation efficiency and drivers of excessive precipitation in post-landfall Hurricane Harvey. *Journal of Hydrometeorology*, *21*(3), 433–452. https://doi.org/10.1175/JHM-D-19-0192.1

Brown, B. R., Bell, M. M., & Frambach, A. J. (2016). Validation of simulated hurricane drop size distributions using polarimetric radar. *Geophysical Research Letters*, *43*(2), 910–917. https://doi.org/10.1002/2015GL067278

Chavas, D. R., Reed, K. A., & Knaff, J. A. (2017). Physical understanding of the tropical cyclone wind-pressure relationship. *Nature Communications*, *8*(1), 1360. https://doi.org/10.1038/s41467-017-01546-9

Cione, J. J., Black, P. G., & Houston, S. H. (2000). Surface observations in the hurricane environment. *Monthly Weather Review*, *128*(5), 1550–1561. https://doi.org/10.1175/1520-0493(2000)128⟨1550:SOITHE⟩2.0.CO;2

Davis, C. A. (2015). The formation of moist vortices and tropical cyclones in idealized simulations. *Journal of the Atmospheric Sciences*, *72*(9), 3499–3516. https://doi.org/10.1175/JAS-D-15-0027.1

Doswell, C. A., Brooks, H. E., & Maddox, R. A. (1996). Flash flood forecasting: An ingredients-based methodology. *Weather and Forecasting*, *11*(4), 560–581. https://doi.org/10.1175/1520-0434(1996)011⟨0560:FFFAIB⟩2.0.CO;2

Emanuel, K. A. (1991). The theory of hurricanes. *Annual Review of Fluid Mechanics*, *23*(1), 179–196. https://doi.org/10.1146/annurev.fl.23.010191.001143

Emanuel, K. A. (1999). Thermodynamic control of hurricane intensity. *Nature*, *401*(6754), 665–669. https://doi.org/10.1038/44326

Fierro, A. O., Rogers, R. F., Marks, F. D., & Nolan, D. S. (2009). The impact of horizontal grid spacing on the microphysical and kinematic structures of strong tropical cyclones simulated with the wrf-arw model. *Monthly Weather Review*, *137*(11), 3717–3743. https://doi.org/10.1175/2009MWR2946.1

Gilford, D. M. (2020). pyPI (v1. 3): Tropical cyclone potential intensity calculations in Python [preprint]. *Geoscientific Model Development Discussions*, 1–30. https://doi.org/10.5194/gmd-2020-279

Gori, A., Lin, N., Xi, D., & Emanuel, K. (2022). Tropical cyclone climatology change greatly exacerbates us extreme rainfall–surge hazard. *Nature Climate Change*, *12*(2), 171–178. https://doi.org/10.1038/s41558-021-01272-7

Guzman, O., & Jiang, H. (2021). Global increase in tropical cyclone rain rate. *Nature Communications*, *12*(1), 5344. https://doi.org/10.1038/s41467-021-25685-2

Hence, D. A., & Houze, R. A., Jr. (2008). Kinematic structure of convective-scale elements in the rainbands of hurricanes katrina and rita (2005). *Journal of Geophysical Research*, *113*(D15). https://doi.org/10.1029/2007JD009429

Hence, D. A., & Houze, R. A., Jr. (2012). Vertical structure of tropical cyclone rainbands as seen by the TRMM precipitation radar. *Journal of the Atmospheric Sciences*, *69*(9), 2644–2661. https://doi.org/10.1175/JAS-D-11-0323.1

Hill, K. A., & Lackmann, G. M. (2009). Influence of environmental humidity on tropical cyclone size. *Monthly Weather Review*, *137*(10), 3294–3315. https://doi.org/10.1175/2009MWR2679.1

Houze, R. A., Jr. (2010). Clouds in tropical cyclones. *Monthly Weather Review*, *138*(2), 293–344. https://doi.org/10.1175/2009MWR2989.1

Houze, R. A., Jr., Rasmussen, K. L., Zuluaga, M. D., & Brodzik, S. R. (2015). The variable nature of convection in the tropics and subtropics: A legacy of 16 years of the Tropical Rainfall Measuring mission satellite. *Reviews of Geophysics*, *53*(3), 994–1021. https://doi.org/10.1002/2015RG000488

Houze, R. A., Jr., Wilton, D. C., & Smull, B. F. (2007). Monsoon convection in the himalayan region as seen by the TRMM precipitation radar. *Quarterly Journal of the Royal Meteorological Society: A Journal of the Atmospheric Sciences, Applied Meteorology and Physical Oceanography*, *133*(627), 1389–1411. https://doi.org/10.1002/qj.106

Hu, J., Rosenfeld, D., Ryzhkov, A., & Zhang, P. (2020). Synergetic use of the WSR-88d radars, GOES-R satellites, and lightning networks to study microphysical characteristics of hurricanes. *Journal of Applied Meteorology and Climatology*, *59*(6), 1051–1068. https://doi.org/10.1175/JAMC-D-19-0122.1

Huang, H., Patricola, C. M., & Collins, W. D. (2021). The influence of ocean coupling on simulated and projected tropical cyclone precipitation in the highresmip–primavera simulations. *Geophysical Research Letters*, *48*(20), e2021GL094801. https://doi.org/10.1029/2021GL094801

Huffman, G. J., Adler, R. F., Bolvin, D. T., & Nelkin, E. J. (2010). The TRMM multi-satellite precipitation analysis (TMPA). In *Satellite rainfall applications for surface hydrology* (pp. 3–22). Springer.

Huffman, G. J., Stocker, E. F., Bolvin, D. T., Nelkin, E. J., & Tan, J. (2019). GPM IMERG final precipitation L3 half hourly 0.1 degree x 0.1 degree V06. (Greenbelt, MD), goddard earth sciences data and information services center (GES DISC), Accessed: February 18,2022) https://doi.org/10.5067/GPM/IMERG/3B-HH/06

Iacono, M., Delamere, J., Mlawer, E., Shephard, M., Clough, S., & Collins, W. (2008). Radiative forcing by long-lived greenhouse gases: Calculations with the AER radiative transfer models. *Journal of Geophysical Research*, *113*(D13). https://doi.org/10.1029/2008JD009944

Iguchi, T., Kozu, T., Kwiatkowski, J., Meneghini, R., Awaka, J., & Okamoto, K. (2009). Uncertainties in the rain profiling algorithm for the TRMM precipitation radar. *Journal of the Meteorological Society of Japan*, *87*, 1–30. https://doi.org/10.2151/jmsj.87A.1

Jiménez, P. A., Dudhia, J., González-Rouco, J. F., Navarro, J., Montávez, J. P., & García-Bustamante, E. (2012). A revised scheme for the wrf surface layer formulation. *Monthly Weather Review*, *140*(3), 898–918. https://doi.org/10.1175/MWR-D-11-00056.1

Jordan, C. L. (1958). Mean soundings for the west indies area. *Journal of the Atmospheric Sciences*, *15*(1), 91–97. https://doi.org/10.1175/1520-0469(1958)015⟨0091:MSFTWI⟩2.0.CO;2

Kanada, S., & Aiki, H. (2024). Buffering effect of atmosphere–ocean coupling on intensity changes of tropical cyclones under a changing climate. *Geophysical Research Letters*, *51*(1), e2023GL105659. https://doi.org/10.1029/2023GL105659

Kim, D., Ho, C.-H., Murakami, H., & Park, D.-S. R. (2021). Assessing the influence of large-scale environmental conditions on the rainfall structure of Atlantic tropical cyclones: An observational study. *Journal of Climate*, *34*(6), 2093–2106. https://doi.org/10.1175/JCLI-D-20-0376.1

Kim, D., Park, D.-S. R., Nam, C. C., & Bell, M. M. (2022). The parametric hurricane rainfall model with moisture and its application to climate change projections. *NPJ Climate and Atmospheric Science*, *5*(1), 86. https://doi.org/10.1038/s41612-022-00308-9

Knutson, T. R., Camargo, S. J., Chan, J. C., Emanuel, K. A., Ho, C.-H., Kossin, J., et al. (2020). Tropical cyclones and climate change assessment: Part II. Projected response to anthropogenic warming. *Bulletin of the American Meteorological Society*, *101*(3), E303–E322. https://doi.org/10.1175/BAMS-D-18-0194.1

Knutson, T. R., Sirutis, J. J., Zhao, M., Tuleya, R. E., Bender, M., Vecchi, G. A., et al. (2015). Global projections of intense tropical cyclone activity for the late twenty-first century from dynamical downscaling of CMIP5/RCP4. 5 scenarios. *Journal of Climate*, *28*(18), 7203–7224. https://doi.org/10.1175/JCLI-D-15-0129.1

Kossin, J. P., Olander, T. L., & Knapp, K. R. (2013). Trend analysis with a new global record of tropical cyclone intensity. *Journal of Climate*, *26*(24), 9960–9976. https://doi.org/10.1175/JCLI-D-13-00262.1

Lai, T.-K., & Toumi, R. (2023). Has there been a recent shallowing of tropical cyclones? *Geophysical Research Letters*, *50*(5), e2022GL102184. https://doi.org/10.1029/2022GL102184

Lavender, S. L., & McBride, J. L. (2021). Global climatology of rainfall rates and lifetime accumulated rainfall in tropical cyclones: Influence of cyclone basin, cyclone intensity and cyclone size. *International Journal of Climatology*, *41*(S1), E1217–E1235. https://doi.org/10.1002/joc.6763

Li, Q., & Wang, Y. (2012). Formation and quasi-periodic behavior of outer spiral rainbands in a numerically simulated tropical cyclone. *Journal of the Atmospheric Sciences*, *69*(3), 997–1020. https://doi.org/10.1175/2011JAS3690.1

Liu, M., Vecchi, G. A., Smith, J. A., & Murakami, H. (2018). Projection of landfalling–tropical cyclone rainfall in the Eastern United States under anthropogenic warming. *Journal of Climate*, *31*(18), 7269–7286. https://doi.org/10.1175/JCLI-D-17-0747.1

Lutsko, N. J., & Cronin, T. W. (2018). Increase in precipitation efficiency with surface warming in radiative-convective equilibrium. *Journal of Advances in Modeling Earth Systems*, *10*(11), 2992–3010. https://doi.org/10.1029/2018MS001482

Martinez, J., Nam, C. C., & Bell, M. M. (2020). On the contributions of incipient vortex circulation and environmental moisture to tropical cyclone expansion. *Journal of Geophysical Research: Atmospheres*, *125*(21), e2020JD033324. https://doi.org/10.1029/2020JD033324

Moon, Y., & Nolan, D. S. (2015). Spiral rainbands in a numerical simulation of hurricane bill (2009). part i: Structures and comparisons to observations. *Journal of the Atmospheric Sciences*, *72*(1), 164–190. https://doi.org/10.1175/JAS-D-14-0058.1

Nakanishi, M., & Niino, H. (2006). An improved Mellor–Yamada level-3 model: Its numerical stability and application to a regional prediction of advection fog. *Boundary-Layer Meteorology*, *119*(2), 397–407. https://doi.org/10.1007/s10546-005-9030-8

Nolan, D. S. (2011). Evaluating environmental favorableness for tropical cyclone development with the method of point-downscaling. *Journal of Advances in Modeling Earth Systems*, *3*(3), M08001. https://doi.org/10.1029/2011MS000063

Onderlinde, M. J., & Nolan, D. S. (2017). The tropical cyclone response to changing wind shear using the method of time-varying point-downscaling. *Journal of Advances in Modeling Earth Systems*, *9*(2), 908–931. https://doi.org/10.1002/2016MS000796

Patricola, C. M., & Wehner, M. F. (2018). Anthropogenic influences on major tropical cyclone events. *Nature*, *563*(7731), 339–346. https://doi.org/10.1038/s41586-018-0673-2

Ramsay, H. A., Singh, M. S., & Chavas, D. R. (2020). Response of tropical cyclone formation and intensification rates to climate warming in idealized simulations. *Journal of Advances in Modeling Earth Systems*, *12*(10), e2020MS002086. https://doi.org/10.1029/2020MS002086

Rasmussen, K. L., & Houze, R. A., Jr. (2011). Orogenic convection in subtropical south America as seen by the TRMM satellite. *Monthly Weather Review*, *139*(8), 2399–2420. https://doi.org/10.1175/MWR-D-10-05006.1

Rasmussen, K. L., & Houze, R. A., Jr. (2016). Convective initiation near the andes in subtropical south America. *Monthly Weather Review*, *144*(6), 2351–2374. https://doi.org/10.1175/MWR-D-15-0058.1

Rasmussen, R., Chen, F., Liu, C., Ikeda, K., Prein, A., Kim, J., et al. (2023). Conus404: The ncar–usgs 4-km long-term regional hydroclimate reanalysis over the conus. *Bulletin of the American Meteorological Society*, *104*(8), E1382–E1408. https://doi.org/10.1175/BAMS-D-21-0326.1

Reed, K. A., Stansfield, A. M., Wehner, M. F., & Zarzycki, C. M. (2020). Forecasted attribution of the human influence on Hurricane Florence. *Science Advances*, *6*(1), eaaw9253. https://doi.org/10.1126/sciadv.aaw9253

Reed, K. A., Wehner, M. F., Stansfield, A. M., & Zarzycki, C. M. (2021). Anthropogenic influence on hurricane dorian's extreme rainfall. *Bulletin of the American Meteorological Society*, *102*(1), S9–S15. https://doi.org/10.1175/BAMS-D-20-0160.1

Reed, K. A., Wehner, M. F., & Zarzycki, C. M. (2022). Attribution of 2020 hurricane season extreme rainfall to human-induced climate change. *Nature Communications*, *13*(1), 1–6. https://doi.org/10.1038/s41467-022-29379-1

Rios Gaona, M. F., Villarini, G., Zhang, W., & Vecchi, G. A. (2018). The added value of imerg in characterizing rainfall in tropical cyclones. *Atmospheric Research*, *209*, 95–102. https://doi.org/10.1016/j.atmosres.2018.03.008

Risser, M. D., & Wehner, M. F. (2017). Attributable human-induced changes in the likelihood and magnitude of the observed extreme precipitation during Hurricane Harvey. *Geophysical Research Letters*, *44*(24), 12–457. https://doi.org/10.1002/2017GL075888

Rotunno, R., & Emanuel, K. A. (1987). An air–sea interaction theory for tropical cyclones. part ii: Evolutionary study using a nonhydrostatic axisymmetric numerical model. *Journal of the Atmospheric Sciences*, *44*(3), 542–561. https://doi.org/10.1175/1520-0469(1987)044⟨0542:AAITFT⟩2.0.CO;2

Schenkel, B. A., Lin, N., Chavas, D., Oppenheimer, M., & Brammer, A. (2017). Evaluating outer tropical cyclone size in reanalysis datasets using QuikSCAT data. *Journal of Climate*, *30*(21), 8745–8762. https://doi.org/10.1175/JCLI-D-17-0122.1

Sena, A. C., Patricola, C. M., Camargo, S. J., & Sobel, A. H. (2024). The atmospheric effect of aerosols on future tropical cyclone frequency and precipitation in the energy exascale earth system model. *Climate Dynamics*, *62*(9), 1–34. https://doi.org/10.1007/s00382-024-07359-z

Shearer, E., Gorooh, V. A., Nguyen, P., Hsu, K.-l., & Sorooshian, S. (2022). Unveiling four decades of intensifying precipitation from tropical cyclones using satellite measurements. *Scientific Reports*, *12*(1), 13569. https://doi.org/10.1038/s41598-022-17640-y

Skamarock, W. C., Klemp, J. B., Dudhia, J., Gill, D. O., Liu, Z., Berner, J., et al. (2019). A description of the advanced research WRF version 4 (Tech. Rep. Nos. TN-556+STR). *National Center for Atmospheric Research Boulder*. https://doi.org/10.5065/1dfh-6p97

Smith, R., & Montgomery, M. (2022). Effective buoyancy and cape: Some implications for tropical cyclones. *Quarterly Journal of the Royal Meteorological Society*, *148*(746), 2118–2131. https://doi.org/10.1002/qj.4294

Sobel, A. H., Camargo, S. J., Hall, T. M., Lee, C.-Y., Tippett, M. K., & Wing, A. A. (2016). Human influence on tropical cyclone intensity. *Science*, *353*(6296), 242–246. https://doi.org/10.1126/science.aaf6574

Song, F., Zhang, G. J., Ramanathan, V., & Leung, L. R. (2022). Trends in surface equivalent potential temperature: A more comprehensive metric for global warming and weather extremes. *Proceedings of the National Academy of Sciences*, *119*(6), e2117832119. https://doi.org/10.1073/pnas.2117832119

Stansfield, A. M. (2025). alyssa-stansfield/wrf-tc-ideal: Final release for accepted manuscript (Version v1) [Computer software]. *Zenodo*. https://doi.org/10.5281/ZENODO.14846073

Stansfield, A. M., & Reed, K. A. (2021). Tropical cyclone precipitation response to surface warming in aquaplanet simulations with uniform thermal forcing. *Journal of Geophysical Research: Atmospheres*, *126*(24). https://doi.org/10.1029/2021JD035197

Stansfield, A. M., & Reed, K. A. (2023). Global tropical cyclone precipitation scaling with sea surface temperature. *NPJ Climate and Atmospheric Science*, *6*(1), 60. https://doi.org/10.1038/s41612-023-00391-6

Stansfield, A. M., Reed, K. A., & Zarzycki, C. M. (2020a). Changes in precipitation from North Atlantic tropical cyclones under RCP scenarios in the variable-resolution community atmosphere model. *Geophysical Research Letters*, *47*(12), e2019GL086930. https://doi.org/10.1029/2019GL086930

Stansfield, A. M., Reed, K. A., Zarzycki, C. M., Ullrich, P. A., & Chavas, D. R. (2020b). Assessing tropical cyclones' contribution to precipitation over the eastern United States and sensitivity to the variable-resolution domain extent. *Journal of Hydrometeorology*, *21*(7), 1425–1445. https://doi.org/10.1175/JHM-D-19-0240.1

Steiner, M., Jr, R. A. H., & Yuter, S. E. (1995). Climatological characterization of three-dimensional storm structure from operational radar and rain gauge data. *Journal of Applied Meteorology and Climatology*, *34*(9), 1978–2007. Retrieved from https://doi.org/10.1175/1520-0450(1995)034⟨1978:CCOTDS⟩2.0.CO;2

Stovern, D. R., & Ritchie, E. A. (2016). Simulated sensitivity of tropical cyclone size and structure to the atmospheric temperature profile. *Journal of the Atmospheric Sciences*, *73*(11), 4553–4571. https://doi.org/10.1175/JAS-D-15-0186.1

Thompson, G., & Eidhammer, T. (2014). A study of aerosol impacts on clouds and precipitation development in a large winter cyclone. *Journal of the Atmospheric Sciences*, *71*(10), 3636–3658. https://doi.org/10.1175/JAS-D-13-0305.1

Tu, S., Xu, J., Chan, J. C., Huang, K., Xu, F., & Chiu, L. S. (2021). Recent global decrease in the inner-core rain rate of tropical cyclones. *Nature Communications*, *12*(1), 1–9. https://doi.org/10.1038/s41467-021-22304-y

Wang, Y. (2009). How do outer spiral rainbands affect tropical cyclone structure and intensity? *Journal of the Atmospheric Sciences*, *66*(5), 1250–1273. https://doi.org/10.1175/2008JAS2737.1

Wang, Y., Lee, K.-H., Lin, Y., Levy, M., & Zhang, R. (2014). Distinct effects of anthropogenic aerosols on tropical cyclones. *Nature Climate Change*, *4*(5), 368–373. https://doi.org/10.1038/nclimate2144

Wei, N., Song, J., Dai, Y., Jiang, S., & Duan, Y. (2022). Recent decrease in inner-core rain rate of tropical cyclones over the western north pacific. *Atmospheric Science Letters*, *e1125*(12). https://doi.org/10.1002/asl.1125

Wing, A. A., Camargo, S. J., & Sobel, A. H. (2016). Role of radiative–convective feedbacks in spontaneous tropical cyclogenesis in idealized numerical simulations. *Journal of the Atmospheric Sciences*, *73*(7), 2633–2642. https://doi.org/10.1175/JAS-D-15-0380.1

Wingo, M. T., & Cecil, D. J. (2010). Effects of vertical wind shear on tropical cyclone precipitation. *Monthly Weather Review*, *138*(3), 645–662. https://doi.org/10.1175/2009MWR2921.1

Wright, D. B., Knutson, T. R., & Smith, J. A. (2015). Regional climate model projections of rainfall from US landfalling tropical cyclones. *Climate Dynamics*, *45*(11–12), 3365–3379. https://doi.org/10.1007/s00382-015-2544-y

Wu, D., Zhang, F., Chen, X., Ryzhkov, A., Zhao, K., Kumjian, M. R., & Chan, P.-W. (2021). Evaluation of microphysics schemes in tropical cyclones using polarimetric radar observations: Convective precipitation in an outer rainband. *Monthly Weather Review*, *149*(4), 1055–1068. https://doi.org/10.1175/MWR-D-19-0378.1

Xi, D., Wang, S., & Lin, N. (2023). Analyzing relationships between tropical cyclone intensity and rain rate over the ocean using numerical simulations. *Journal of Climate*, *36*(1), 81–91. https://doi.org/10.1175/JCLI-D-22-0141.1

Xu, Z., Ji, F., Liu, B., Feng, T., Gao, Y., He, Y., & Chang, F. (2021). Long-term evolution of global sea surface temperature trend. *International Journal of Climatology*, *41*(9), 4494–4508. https://doi.org/10.1002/joc.7082

Yu, C.-K., Lin, C.-Y., & Pun, C.-H. (2023). Origin of outer tropical cyclone rainbands. *Nature Communications*, *14*(7061), 7061. https://doi.org/10.1038/s41467-023-42896-x

Yu, H. (2022). Cloud_system_classification: V1.0 (v1.0). *Zenodo*. https://doi.org/10.5281/zenodo.6491939

Zhang, C., & Wang, Y. (2017). Projected future changes of tropical cyclone activity over the western north and south pacific in a 20-km-mesh regional climate model. *Journal of Climate*, *30*(15), 5923–5941. https://doi.org/10.1175/JCLI-D-16-0597.1